

Simulations of the merging cluster of galaxies Cygnus A

T. L. R. Halbesma,^{1,2*} J. M. F. Donnert,^{3,4} M. N. de Vries,^{1,5} M. W. Wise^{1,5}

¹*Astronomical Institute “Anton Pannekoek”, University of Amsterdam, Science Park 904, 1098 XH Amsterdam, The Netherlands*

²*Max Planck Institute for Astrophysics, Karl-Schwarzschild-Str. 1, D-85741 Garching, Germany*

³*INAF Istituto di Radioastronomia, via P. Gobetti 101, I-40129 Bologna, Italy*

⁴*University of Minnesota, School of Physics and Astronomy, 116 Church St SE, MN 55455 Minneapolis, USA*

⁵*ASTRON, Netherlands Institute for Radio Astronomy, Postbus 2, 7990 AA, Dwingeloo, The Netherlands*

Accepted 2018 December 10. Received 2018 December 10; in original form 2018 July 24

ABSTRACT

The archetype FR-II galaxy Cygnus A lies in a moderately rich cluster about to undergo a major merger. We study the pre-merger Cygnus cluster environment using smoothed particle hydrodynamics simulations constrained by 2Ms of *Chandra* observations of the hot intracluster medium. The observations constrain the total gravitating mass and concentration parameter, and the simulations provide the quiescent and merger-enhanced temperature profiles of the pre- and post merger of the cluster excluding the central active galactic nucleus. We present the first detailed model of the sub cluster north west of Cygnus A, named CygNW. We find a lower baryon fraction and higher concentration parameter for CygA than expected from known scaling relations in the literature. The model suggests the Cygnus cluster hosts a pre-merger with a progenitor mass ratio of about 1.5:1 at the virial radius. We notice that the intra cluster medium is heated as a result of the merger, but we find no evidence for a (pre-)merger shock in the interstitial region between both cluster haloes. We attribute the merger-induced heating to compression of the cluster outskirts. The smooth model obtained from our simulations is subtracted from the observed cluster state and shows residual temperature structure that is neither hydrostatic nor merger-heated cluster gas. We speculate that this residual heating may result from previous AGN activity over the last ~ 100 Myr.

Key words: galaxies: clusters: individual: Cygnus A – galaxies: clusters: intracluster medium – X-rays: galaxies: clusters – X-rays: individual: Cygnus A – galaxies: active

1 INTRODUCTION

Cluster mergers, gas cooling, and galaxy feedback dominate the energetics of galaxy clusters in the current epoch. Mergers are expected throughout cosmic time in the paradigm of hierarchical structure formation, while feedback becomes energetically important from redshift $z = 2$ onwards (e.g. Somerville & Davé 2015). Active Galactic Nuclei (AGN) provide one type of such feedback. The Cygnus cluster prominently shows signatures of AGN feedback as the brightest cluster galaxy (BCG) hosts the FR-II source Cygnus A. In addition, the subcluster that this radio source is confined in is about to undergo a major merger (Sarazin et al. 2013). Therefore, the Cygnus cluster provides a unique opportunity for an in-depth study of relative cluster energetics. Moreover, its proximity and extreme X-ray brightness combined with newly obtained, deep observations obtained at the excellent

spatial resolution of *Chandra* allows for a detailed study of the inner region directly surrounding Cygnus A as well as a study of the Cygnus cluster environment.

The well-known radio galaxy Cygnus A has been studied extensively the last decades (e.g. Carilli & Harris 1996; Carilli & Barthel 1996). The radio emission originates from accretion onto a supermassive black hole (SMBH) in the BCG of the Cygnus cluster with an estimated black hole mass of $(2.5 \pm 0.7) \times 10^9 M_{\odot}$ (Tadhunter et al. 2003). Notable X-ray features as a result of interaction of Cygnus A with the surrounding cluster gas are seen inside the cocoon shock in the inner 30 – 60 kpc of the cluster. The central region shows two distinct X-ray jets with hot spots at the jet termini that can be used to estimate the AGN output energy. Other measurements of the AGN energetics include computations of the work required to create the observed X-ray cavities and, conversely, regions of higher density. The previous deepest X-ray observation to date focussing on the large-scale structure of the Cygnus cluster is analysed by

* E-mail: halbesma@MPA-Garching.MPG.DE

Smith et al. (2002), and more recent work on the inner region can be found in Steenbrugge et al. (2008, and companion papers), Yaji et al. (2010), and Chon et al. (2012).

The moderately rich Cygnus cluster in and of itself is also interesting and well-studied. First reported as a powerful X-ray source in the *Uhuru* catalog (Giacconi et al. 1972), the system has been observed by every major mission since. An early rough mass estimate of $10^{14} M_{\odot}$ is given by Fabiano et al. (1979) and confirmed by Arnaud et al. (1984, 1987). The authors further report that Cygnus A lies in a cool core cluster (at the time called ‘a cluster with a strong cooling flow’), and a β -model (Cavaliere & Fusco-Femiano 1978) fit to the intra cluster medium (ICM) density profile yields a central density of 0.02 cm^{-3} . Moreover, these observations show a plume of hot intracluster gas extending to the north west, later confirmed by Carilli et al. (1994), and now known to be a distinct subcluster. X-ray observations show that the cool-core cluster is undergoing a major merger with the subcluster to the north west.

Markevitch et al. (1999) reported detection of a higher temperature in the region in-between both subclusters, indicative of a head-on pre-merger between (apart from the cool core in Cygnus A) two nearly equal 4 – 5 keV clusters that drives a merger shock into the ICM. Sarazin et al. (2013) further studied the merger shock based on these data supplemented with *Suzaku* observations. The latter shows an increase in redshift of Fe K line emission along the presumed merger axis¹. This increment is interpreted as a Doppler shift indicating that the cluster to the north west is on the foreground with respect to- and falling in towards Cygnus A. The measured radial component of the merger velocity is $2650 \pm 900 \text{ km/s}$, and the collision velocity is estimated from the temperature jump as 2400 – 3000 km/s. Combining both yields an inferred angle between the merger-axis and the line-of sight of 54° .

Dynamical modelling of optical observations shows an Abell richness of the cluster of 2 – 4, a velocity dispersion of $1581_{-197}^{+286} \text{ km/s}$, and indicates that the dynamical center of the spatial distribution is offset to the north west of Cygnus A, and the Cygnus A galaxy has a redshift of $z = 0.0562$ (Owen et al. 1997). The dynamical model supports the pre-merger state of the cluster estimated around 200 – 600 Myr prior to core passage where the distance between both haloes is $460h_{75}^{-1} \text{ kpc}$ based on the galaxy surface density peaks, and the system is seen at an inclination of 30 – 45° (Ledlow et al. 2005). The authors further provide mass-estimates computed using a projected mass estimator $M_{\text{PME}} = 4.4 \times 10^{15} M_{\odot}$, and from virial theorem $M_{\text{VT}} = 3.0 \times 10^{15} M_{\odot}$. Prior literature indicates that the Cygnus cluster hosts a major merger with a mass ratio of 2-3:1. To our knowledge, no weak-lensing studies or deeper optical observations of the cluster environment have been published to date.

One of the challenges with our new observations (Wise et al. in prep, see Section 2 below) is to differentiate between the contribution of the merger on the one hand, and on the other hand the effects of AGN output over the past several hundred megayears in the same set

of observations. To assist interpreting the data we run idealised binary merger simulations of the ongoing merger in the Cygnus cluster where we exclude the AGN and its effect on the ICM. The simulations can constrain the quiescent hydrostatic temperature of the ICM as well as merger-heated temperature profiles. The goal is to understand the Cygnus cluster environment, particularly the properties of both merging subclusters as well as the energetics of the merger.

Newly obtained, detailed radial profiles of both subclusters constrain the properties of the merger in the Cygnus cluster. We adopt the relevant *Chandra* observations from Wise et al. (in prep) that are obtained as part of a recent multi-wavelength observational campaign of persistent AGN activity in the merging Cygnus cluster in section 2. The X-ray observations as well as the optical dynamical model suggest a head-on merger between two nearly equal clusters of galaxies. This is also seen in the newly obtained deep *Chandra* observations. Our cluster model and the inferred halo parameters are presented in section 3, followed by the numerically sampled clusters in section 4. We present simulations of the head-on merger scenario in section 5 and discuss the interpretation of the simulations in section 6. We conclude in section 7.

Throughout this paper we assume a concordance Λ CDM cosmology with $H_0 = 70 \text{ km/s/Mpc}$, $\Omega_{\Lambda} = 0.7$, and $\Omega_{\text{M}} = 0.3$. This yields an angular diameter of $1'' \sim 1.091 \text{ kpc}$ and a critical density of $\rho_{\text{crit}} = 9.7 \times 10^{-30} \text{ g/cm}^3$ at the redshift of the Cygnus cluster.

2 CHANDRA CONSTRAINTS ON THE CYGNUS MERGER SIMULATIONS

New *Chandra* ACIS observations of the Cygnus cluster were obtained as part of a recent multi-wavelength observational campaign (Wise 2014). An overview of the data analysis of the two mega seconds of *Chandra* data is outlined by Wise et al. (in prep). A detailed discussion of the non-thermal emission originating from the central region surrounding the AGN is published by de Vries et al. (2018). McKean et al. (2016) analysed LOFAR data on the emission originating from the hotspots at the jet termini, and Perley et al. (2016) obtained new JVLA observations of Cygnus A.

2.1 X-ray map of the Cygnus cluster

The left panel of Figure 1 shows the *Chandra* X-ray surface brightness (0.5 – 7.0 keV) with a total exposure time of 2.2 Msec. The Cygnus cluster hosts two distinct sub clusters. We refer to as the sub cluster that the radio source Cygnus A is confined as ‘CygA’, and following Wise et al. (in prep), the distinct subcluster to the north west is named ‘CygNW’. CygA appears roughly spherical although departure from perfect spherical symmetry in the direction of the western jet can be seen. CygNW appears slightly elongated towards - and is much fainter than - CygA. In fact, CygNW is only visible after significant smoothing with a $\sigma = 9$ pixels ($0.492''/\text{pixel}$) Gaussian smoothing kernel.

We focus on the interstitial region in particular where we observe filamentary structure. This excess surface brightness in-between CygA and CygNW is clearly seen along the

¹ The dashed line in Figure 1 (left) shows the projected merger-axis.

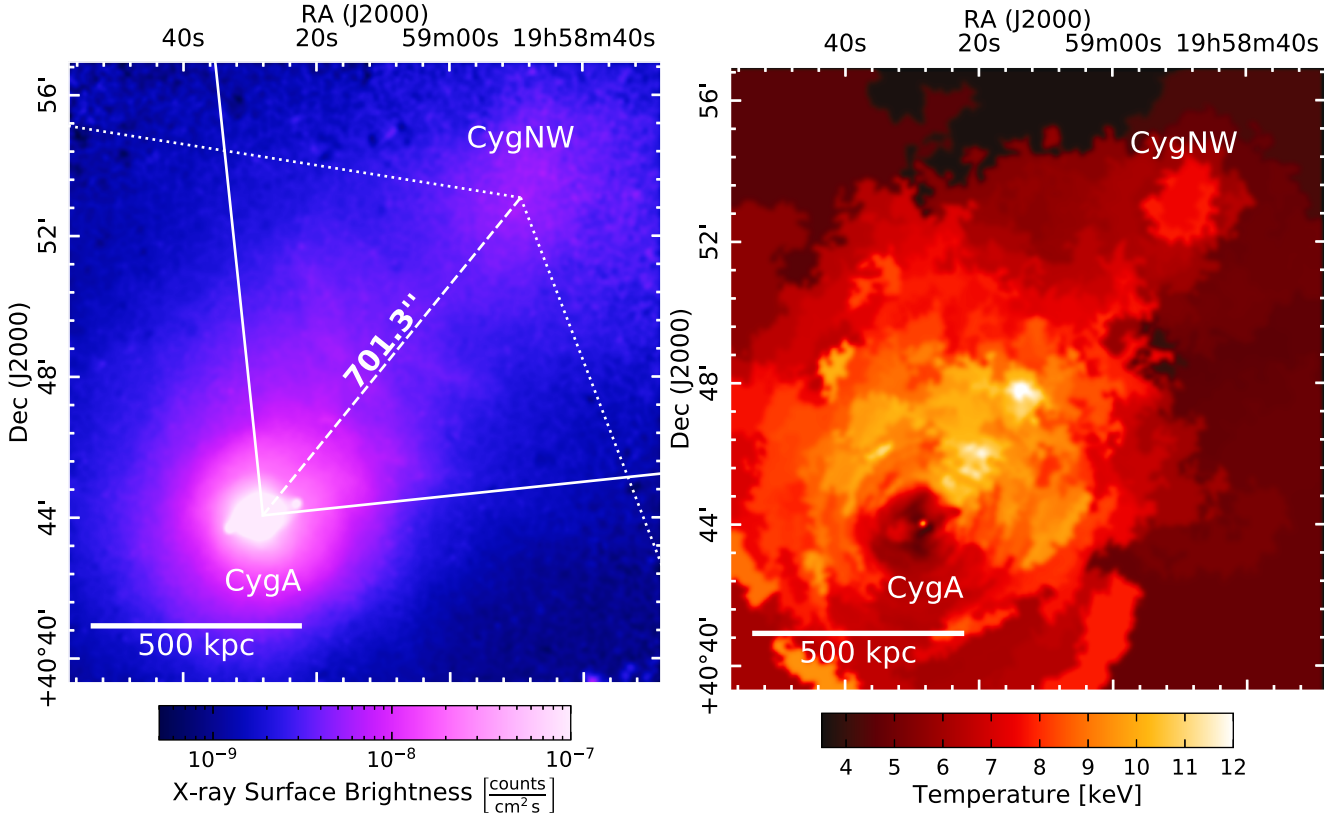


Figure 1. *Left:* X-ray surface brightness (*Chandra* ACIS, 0.5 – 7.0 keV, 2.2 Msec of exposure), convolved with a Gaussian smoothing kernel ($\sigma = 9$ pixels, $0.492''/\text{pixel}$). We show a log stretch zoomed-in on the interstitial region. The dashed line shows a projection of the presumed merger axis to a measured core separation of $701.3'' \sim (765 h_{70}^{-1} \text{ kpc})$. Excess emission is seen in-between the two haloes. The solid lines mark the boundaries of the wedges used to extract radial profiles for CygA, and the dotted line indicates these regions for CygNW. *Right:* Observed temperature map in keV smoothed with a 9σ Gaussian.

presumed merger-axis (indicated by the dashed line). In this work we investigate whether the excess could be merger-induced or signatures of previous AGN activity. The measured projected core separation, the distance between both halo centroids, is $701.3'' \sim (765 h_{70}^{-1} \text{ kpc})$.

2.2 Temperature structure

The temperature structure of the Cygnus cluster is presented in Figure 1 (right). Wise et al. (in prep) presents a detailed description of the reduction and analysis of the observations; here we summarise the key aspects. All observations are reprocessed with CIAO 4.9 and CALDB 4.7.4 (Fruscione et al. 2006). The observed temperature map is created using the CONTBIN algorithm (Sanders 2006) to generate two-dimensional bins. CONTBIN requires that each bin has a surface brightness with a constant signal-to-noise ratio of 75 and increases the bin until this condition is met.

For each bin *specextract* is used to extract spectra, and the SHERPA (Freeman et al. 2001) fitting package within CIAO is then used to spectral fit a single-temperature APEC model (Smith et al. 2001) multiplied with a TBABS absorption model (Wilms et al. 2000). A column density of $N_H = 3.1 \times 10^{21} \text{ cm}^{-2}$ for absorption due to neutral hydrogen in the Galactic plane is obtained by averaging values adopted from the Leiden/Argentine/Bonn (LAB) (Kalberla et al. 2005) and Dickey & Lockman (1990) surveys. Finally,

we convolve the resulting temperature map with a Gaussian kernel ($\sigma = 9$) to smooth over AGN interactions in the central regions while simultaneously enhancing the cluster-scale features. The cool core of CygA is visible in the temperature map, while the central region of CygNW is hot compared to its direct surroundings.

2.3 Beta model fit to *Chandra* radial profiles

Radial profiles are extracted by Wise et al. (in prep); here we summarise the relevant steps in the data reduction only. The interstitial region of enhanced surface brightness is cut out in efforts to create ‘quiescent’ radial profiles of CygA and CygNW. This is done to minimise contamination of whichever physical phenomenon causes the excess emission. The solid lines centered on CygA mark the two regions used to extract the radial profiles. The wedge enclosing the merger-axis is coined the ‘merger-region’ and spans $6 - 96^\circ$ measured from west to the north, while its inverse is dubbed the ‘quiescent’ or average region. The dotted lines around the merger-axis indicates the region cut out to obtain the quiescent radial profile of CygNW.

Wise et al. (in prep) subdivide each wedge in partial annuli, bin them in such a way that each annulus contains the same number of counts. Finally, the authors fit an APEC model to the extracted spectra to obtain the density and temperature values. The adaptive binning algorithm re-

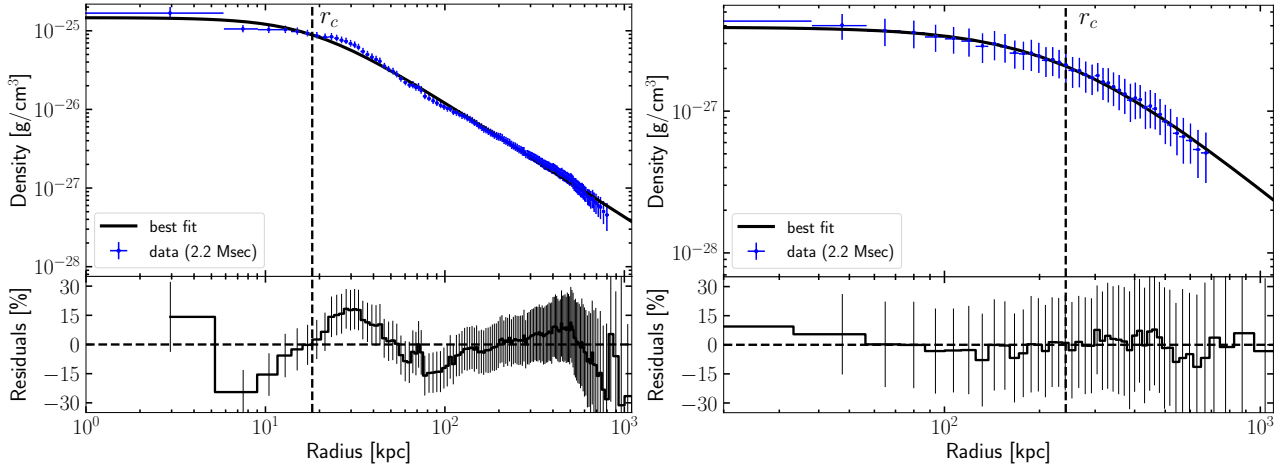


Figure 2. β -model fit to the observed, adaptively-binned X-ray surface brightness wedge excluding the merger-axis, centered on CygA (left) and CygNW (right).

Table 1. Best fit parameters used as initial conditions to set up numerical representations of the CygA and CygNW haloes. The β -model parameters are constrained by the *Chandra* density profile, while the remaining quantities are inferred by fitting the total hydrostatic temperature (assuming dark matter follows the NFW-profile) to the observed temperature profile. We use the model with an additional cut-off in the NFW-profile and β -model. The value $c_{\text{NFW}}(M_{200})$ is computed using the scaling relation of [Duffy et al. \(2008\)](#).

Parameter		CygA	CygNW
ρ_0	(10^{-26} g/cm 3)	14.68 ± 0.61	0.39 ± 0.01
r_c	(kpc)	18.22 ± 0.78	242.1 ± 9.86
β		0.486 ± 0.004	0.608 ± 0.02
$\chi^2_{\text{min}}/\text{dof}$		63.6 / 127	1.4 / 39
$\rho_{0\text{dm}}$	(10^{-25} g / cm 3)	1.82	0.23
c_{NFW}		7.18	2.87
$c_{\text{NFW}}(M_{200})$		3.35	3.48
$b_f f_{200}$	(per cent)	7.01	7.35
M_{200}	(10^{14} M_{\odot})	7.36	4.99
$M_{200\text{gas}}$	(10^{14} M_{\odot})	0.52	0.37
M_{500}	(10^{14} M_{\odot})	5.66	3.16
r_{200}	(kpc)	1831	1609
r_{500}	(kpc)	1235	1018
r_s	(kpc)	255.0	560.9
r_{sample}	(kpc)	6865	2413
r_{cut}	(kpc)	854.7	987.3

quires a signal-to-noise ratio of 273 (75) for CygA (CygNW), thus the radial profiles have uniform error bar sizes. We present our β -model ([Cavaliere & Fusco-Femiano 1978](#)) fit to the radial profile within the ‘quiescent’ wedge in [Figure 2](#) for CygA (left panel) and for CygNW (right panel). The best fit β -model parameters are presented in [Table 1](#) (top).

3 CLUSTER MODEL

We adopt the cluster model of [Donnert \(2014, hereafter D14\)](#) and [Donnert et al. \(2017, D17\)](#). D17 use the [Navarro, Frenk & White \(1995, NFW\)](#) profile to describe the dark matter density as a function of radius. An additional cut-off is used

because the profile does not converge for $r \rightarrow \infty$. The integral with the cut-off density profile has to be solved numerically. The expression for the cutoff NFW density is

$$\rho_{\text{dm}}(r) = \rho_{0\text{dm}} \left[\frac{r}{r_s} \left(1 + \frac{r}{r_s} \right)^2 \right]^{-1} \left[1 + \left(\frac{r}{r_{\text{sample}}} \right)^3 \right]^{-1}, \quad (1)$$

where r_s is the scaling radius, and $\rho_{0\text{dm}}$ is a scaling parameter for the density profile. As per D14, the sample radius r_{sample} is set to half the size of the simulation box, $L_{\text{box}} = 3.75 r_{200}$ for the primary halo (CygA), and to $1.5 r_{200}$ for the additional halo (CygNW). The virial radius r_{200} is defined as the radius at which the average (spherical) density equals two hundred times the critical density of the Universe at the redshift of the cluster. The concentration parameter of the dark matter halo is defined as the ratio of the virial radius to the scaling radius, $c_{\text{NFW}} = r_{200}/r_s$, and is a free parameter in our fit.

The baryonic content of clusters consists of the intra cluster medium and the stellar component. We neglect the latter, and for the ICM we define the baryon fraction as $b_f = M_{\text{gas}}/(M_{\text{gas}} + M_{\text{dm}})$ and the gas density profile follows the β -model ([Cavaliere & Fusco-Femiano 1978](#)). D17 adopt an additional cut-off in the β -model to ensure that the local baryon fraction in the numerical implementation stays below unity throughout the simulation box for stability, with

$$\rho_{\text{gas}}(r) = \rho_{0\text{ICM}} \left[1 + \left(\frac{r}{r_c} \right)^2 \right]^{-3\beta/2} \cdot \left[1 + \left(\frac{r}{r_{\text{cut}}} \right)^3 \right]^{-1}, \quad (2)$$

with core radius r_c and power-law slope β outside the core. The cut-off radius is parametrized as a fraction of the virial radius, where D17 finds $r_{\text{cut}}/r_{200} \sim 1.7$ in the Perseus cluster.

Finally, D14 and D17 assume that both progenitors are spherically symmetric and in hydrostatic equilibrium where self-gravity is balanced by gas pressure.

3.1 Progenitor properties

We adopt the view that the Cygnus cluster is in a pre-merger state roughly 200 – 600 Myr prior to core passage ([Ledlow et al. 2005](#)). The undisturbed X-ray morphology and

the prominent cool core of CygA further supports the pre-merger conclusion (Ledlow et al. 2005). We thus assume that the progenitor haloes are described by the current observations, specifically by the radial profiles within the quiescent wedge.

In addition to the radial density profiles already presented in Figure 2, Wise et al. (in prep) has also extracted radial temperature profiles. We first compute the total gravitating mass from the observed density profile by assuming a fixed baryon fraction at the virial radius. The temperature profile then follows from hydrostatic equilibrium, and the pressure can be computed by adopting the ideal gas law as an equation of state. We χ^2 fit the computed hydrostatic temperature profile to the observed temperature profile where the free parameters are r_{200} , c_{NFW} , and b_f . Decreasing the baryon fraction results in a higher overall temperature of the cluster, while the concentration parameter determines the amount of dark matter within the scaling radius. The latter effectively shifts the peak of the temperature profile inward or outward by respectively increasing or decreasing the concentration parameter. For CygA we only take into account $50 \text{ kpc} < r < 500 \text{ kpc}$. The cocoon shock around Cygnus A is observed in the inner $\sim 30 - 60 \text{ kpc}$ (depending on the direction), thus, the temperature structure in this region is highly influenced by the AGN rather than only showing the hydrostatic temperature of the cluster.

Based on these observations we find β -model properties for CygA that are consistent with earlier findings of Smith et al. (2001), who reported $r_c \approx 18''$ (19.3 kpc), $\beta \approx 0.51$ for the cluster gas in the inner $300''$. We find a core radius of $18.23 \pm 0.78 \text{ kpc}$, $\beta = 0.486 \pm 0.004$ within 1 Mpc. Furthermore, in order to match the hydrostatic temperature to the observed temperature profile we find a low baryon fraction and high concentration parameter of $b_{f200} = 7.0 \%$ and $c_{\text{NFW}} = 7.18$. Using the Duffy et al. (2008) scaling relation between the concentration parameter and total mass, we expect a value of $c_{\text{NFW}}(M_{200}) \sim 3.35$. Although the scaling relation is not tightly constrained, the concentration that we find for CygA falls in the upper part of the scatter in the scaling relation. A baryon fraction of $0.039 - 0.055$ has previously been reported by Smith et al. (2001), a bit lower than our findings.

The progenitor properties are presented in Section 4. Table 1 shows the inferred parameters with the additional cut-off in the density profiles. Our mass estimate is given at two characteristic radii, both at the virial radius r_{200} and at r_{500} to assist comparing the Cygnus cluster haloes with known scaling relations in the literature. The corresponding radial profiles are plotted in Figure 4 for CygA, respectively Figure 5 for CygNW. The observed data points are shown in blue. The upper and lower right panel show the hydrostatic mass and pressure, both of which are computed from the observed density and temperature profiles. The black lines show the analytical profiles where we note that the β -model and hydrostatic temperature are fitted to the observations. The mass- and pressure profiles self-consistently lie on top of the respective observed profiles. Finally, the green points show the numerically sampled profiles which we further address in section 4.

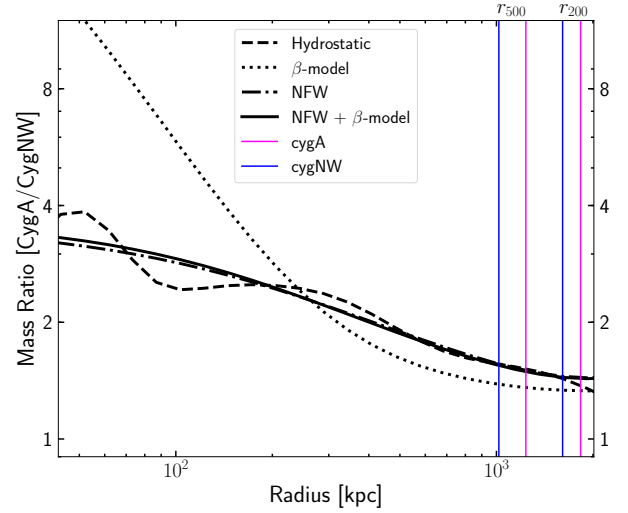


Figure 3. Mass ratio as computed from the observations (hydrostatic mass equation, dashed line) versus the mass ratio found by modelling the cluster environment. The solid line shows the ratio of total mass while the baryonic and dark mass ratio is shown by the dotted, respectively, dash-dotted line. The vertical lines show r_{500} and r_{200} of CygA (magenta), and CygNW (blue). Note that the virial radii lie well outside the observed data range.

3.2 Mass ratio

The dynamical model of Ledlow et al. (2005) shows that the mass ratio in the Cygnus cluster is at most of order 2:1, where CygA is the more massive cluster. Our modeling, on the other hand, suggests that the progenitors have a mass ratio of **1.5:1** at the virial radius r_{200} as seen in Table 1. We show the mass ratio as a function of radius in Figure 3.

Following Wise et al. (in prep), we adopt the hydrostatic mass profile of Fabricant et al. (1980, eq. 6) to compute the observed total mass as a function of radius given the observed density and temperature profiles and their derivatives. We obtain the latter by smoothing the observed profiles, fitting a cubic spline and taking the derivative of the spline. We show the resulting mass ratio with a dashed line and note that the adopted equation only assumes hydrostatic equilibrium and spherical symmetry, but requires no assumptions for the shape of the dark matter halo. The dotted line shows the mass ratio of the baryons in the ICM, and the mass ratio of the dark component is shown by the dash-dotted line where we assume that the dark matter halo is described by the NFW-profile. We note that the inferred virial radii fall well outside the range of observed radii, and the sum of the virial radii of CygA and CygNW is significantly larger than the observed core separation, further discussed in section 6.

4 INITIAL CONDITIONS

The cluster model is implemented in the OPENMP parallel code TOYCLUSTER², first presented by D14 while the latest

² <https://github.com/jdonnert/Toycluster>

changes are published in D17. Two minor modifications with respect to the latter have been made for our purposes to sample the initial conditions for CygA and CygNW as given in Table 1. We allow for an individual baryon fraction for both haloes, and for different cut-off radii per halo to have our fiducial cluster match the observations as accurately as possible.

The initial Poisson sampling error of order 21% is reduced to $< 3\%$ as the result a relaxation loop based on the weighted voronoi tessellation (WVT) algorithm of Diehl et al. (2012). In each relaxation step a fiducial force is computed to push particles apart to improve the particle sampling and reduce the mean sampling error, see D17 and Arth et al. (in prep) for details. Individual clusters are then stable under hydrostatic equilibrium for more than 5 Gyr. Moreover, the numerically sampled profiles follow the analytical requirements without much scatter as a result of the WVT relaxation. The numerically sampled radial profiles are shown as the green points and lines in Figure 4 for CygA, respectively, Figure 5 for CygNW. The mean smoothing length of the particles within the inner 100 kpc is shown as a vertical dotted green line to indicate the kernel resolution scale. The shaded grey area indicates the boundary region where the model is no longer valid.

4.1 Progenitor orbit

We sample the cluster with desired parameters in a simulation box and place the haloes on a collision course assuming that the merger trajectory is described by a parabolic orbit.

Following D17, the initial velocity is parametrized using the zero-energy orbit fraction X_E . This parameter lies between zero and one. The value $X_E = 0$ corresponds to the case where both clusters are initially at rest at infinite distance. Conversely, for $X_E = 1$ all available potential energy is converted to kinetic energy. The first relevant snapshot of the simulations is when the merger starts. Therefore both haloes are placed in the box at a distance such that their virial radii touch. No hard constraints on the impact parameter are given in the literature, but the merger scenario of Markevitch et al. (1999) suggests a head-on collision. For this reason the impact parameter of the Cygnus merger simulations is set to zero (head-on). Although we are not bound to this assumption, we did not further investigate this parameter due to the lack of observational constraints. Three initial merger velocities are chosen with values of $X_E \in [0.25, 0.50, 0.75]$, thus, three different initial condition files are generated. This corresponds to an approach velocity $v_{\text{initial}} \in [650, 1301, 1952]$ km/h. For all simulations we also investigate the inclination i of the system. A value of $i = 0^\circ$ corresponds to the merger occurring in the plane of the sky, while $i = 90^\circ$ indicates a merger along the line of sight. The inclination angle can be chosen after the simulation run to create two-dimensional projections of physical quantities as part of the post-processing. We chose to investigate the temperature structure of the simulated cluster for inclination angles of $i \in [0, 15, 30, 45, 60, 75]$. The resulting merger simulations are presented in the following section.

5 RESULTS

We use the TREE-SPH code GADGET3 (Springel 2005; Dolag & Stasyszyn 2009; Beck et al. 2016a) with the bias-corrected Wendland C6 kernel with 295 ± 0.01 neighbours (Dehnen & Aly 2012). The simulation runs are performed on the Dutch Compute Cluster Lisa and on the Freya compute cluster at the Max Planck Computing and Data Facility (MPCDF), using 20 million particles split up equally between the dark matter and the gas particles. This results in an effective mass resolution of $9.84 \times 10^6 M_\odot$ for SPH, and $1.77 \times 10^8 M_\odot$ for DM particles. Snapshots are written every 10 Myr for a simulation run of 3 Gyr without comoving integration as the redshift of the Cygnus cluster is 0.0562, and the gravitational softening is set to one seventh of the mean particle separation, or 3.61 kpc.

Temperature increase and puff-up

We confirm that both clusters are stable over the course of the simulation by plotting the radial profiles of both haloes at every time step. We notice that the temperature profile in the inner ~ 300 kpc of fiducial CygA rapidly increases by $\sim 10\%$ during the first ~ 230 Myr of the simulation run. After this initial rapid increase the temperature profile stabilises. The temperature of CygNW ($r < 50$ kpc) also increases slightly, but remains within the *Chandra* errorbars. The increase in central temperature is not observed when both fiducial subclusters are sampled individually (i.e. in their own simulation box).

In addition, the scatter of the temperature profile increases over the course of the simulation run although the initial conditions started with radial profiles that closely follow the analytical profiles without much scatter as a result of the WVT relaxation step. The density, on the other hand, remains well-constrained with a small scatter.

Both effects can be seen in Figure 6 where we show the $X_E = 0.50$ simulation 230 Myr after starting the simulation run, which is the last snapshot before the central temperature of fiducial CygA stabilises in this simulation. In this figure we can also see an increased temperature around 1 – 2 Mpc. The interstitial region between fiducial CygA and CygNW sits at these radii where the ICM is heated as a result of the merger. Finally we would like to draw attention to the green dotted vertical line showing the kernel scale radius. The hot core of CygNW lies well within the kernel, meaning that this region is represented by too few SPH particles to be well resolved numerically. As a result, the high-temperature core of CygNW is washed out in our simulations and the temperature structure will be too cold in comparison to the observations later on.

Selecting suitable simulation snapshots

The measured core separation further constrains our simulations of the Cygnus cluster, in addition to the (already) matching radial profiles. We compute the core separation for each snapshot of all three initial velocities, and resimulate those closest to a projected distance of ~ 765 kpc for the six inclination angles. The finer interpolation writes snapshots at a forty times higher rate (i.e. every 0.25 Myr) to obtain a fiducial core separation as close to the observation

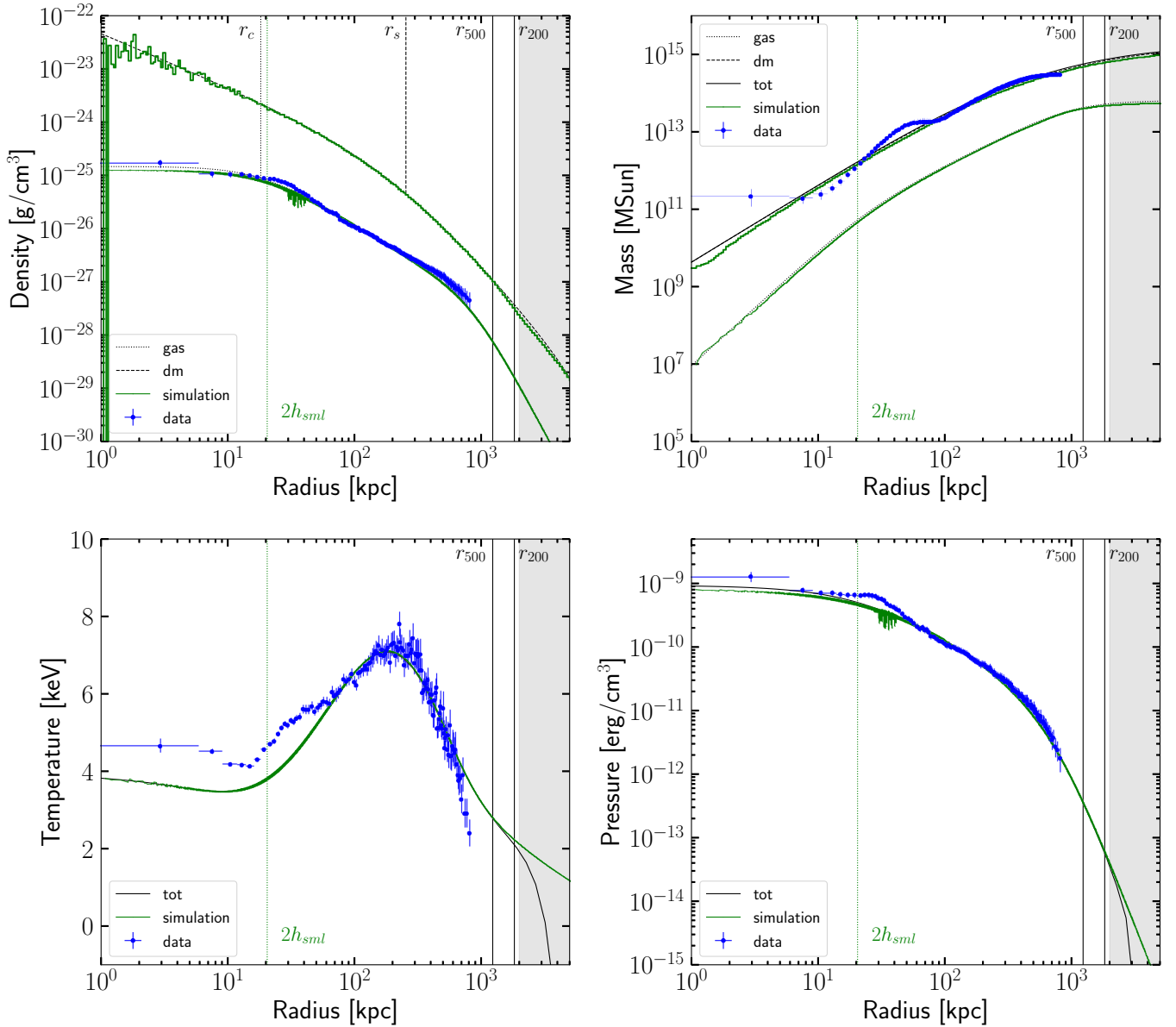


Figure 4. Comparison between fiducial radial profiles of CygA of the initial conditions (shown in green) and the observed ‘quiescent’ radial profiles (blue). We show the density profile (upper left), mass profile (upper right), temperature profile (lower left), and pressure profile (lower right). The β -model is fitted to the observed density profile, and the dark matter (NFW) profile is inferred under the assumption of a fixed baryon fraction at the virial radius r_{200} . The core radius of the β -model and the scaling radius of the NFW profile are indicated by the vertical dotted, respectively, dashed line, and the vertical green line indicates the resolution scale.

as possible. Note that we adopt the distance between CygA and CygNW as seen in our *Chandra* observation rather than using the (much smaller) value found in the optical dynamical model. We do so because i) the optical core separation is obtained from the galaxy surface density peaks, but the optical galaxy distribution is sparse, ii) reproducing the optical surface density showed us that the level of smoothing the galaxy distribution strongly affects the peak location, and iii) the simulated X-ray surface brightness is compared to the observed X-ray surface brightness.

A degeneracy exists between the initial (merger) velocity and the inclination angle. We can use the amount of the merger heating to select which one of the snapshots best-

represents the observed cluster state. As seen in Figure 6 in the 1 – 2 Mpc region, the merger will heat the ICM in-between fiducial CygA and CygNW. If the clusters approach one another with a higher velocity, the cluster gas will be prone to more heating than for lower-velocity simulations. At the same time, increasing inclination angles correspond to a higher physical separation, thus, the cluster gas will have undergone less heating and the merger-induced heating will be less profound.

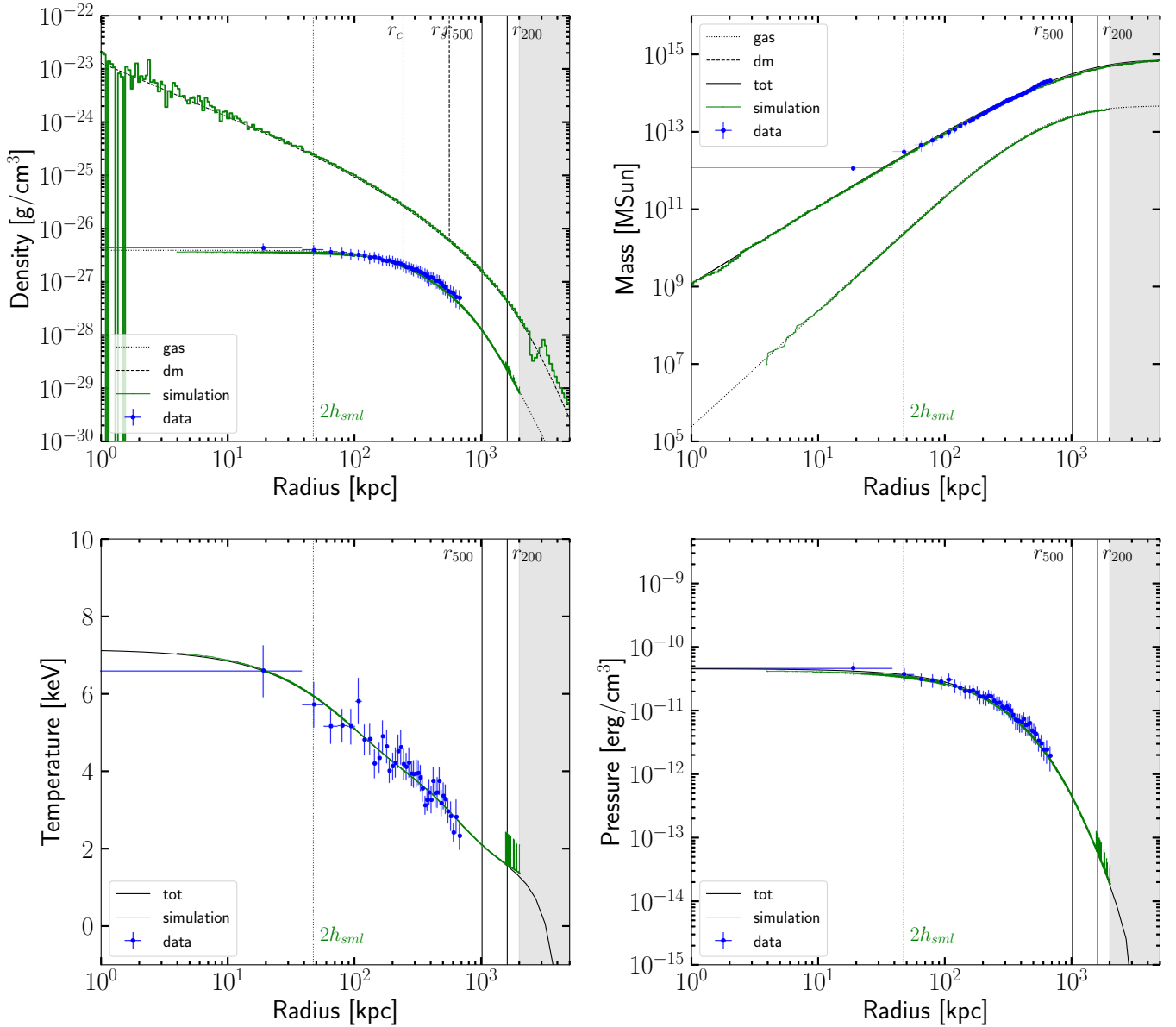


Figure 5. Comparison between fiducial radial profiles of CygNW of the initial conditions (shown in green) and the observed ‘quiescent’ radial profiles (blue). We show the density profile (upper left), mass profile (upper right), temperature profile (lower left), and pressure profile (lower right). The β -model is fitted to the observed density profile, and the dark matter (NFW) profile is inferred under the assumption of a fixed baryon fraction at the virial radius r_{200} . The core radius of the β -model and the scaling radius of the NFW profile are indicated by the vertical dotted, respectively, dashed line, and the vertical green line indicates the resolution scale.

5.1 X-ray surface brightness and temperature

Figure 7 shows the combinations of different values for the inclination and initial velocity as adopted in this study. The

selected snapshots are post-processed with P-SMAC2³ (Donnert & Brunetti 2014) to generate two dimensional line-of-sight integrated X-ray surface brightness and temperature maps. The former shows a computation of the projected thermal bremsstrahlung continuum emission, adopting Bartelmann & Steinmetz (1996, eq. 3) and selecting an energy range of 0.5 – 7.0 keV to match the *Chandra* energy band used to create the observed mosaic. The latter shows our computations of the projected spectroscopic temperature where we use the model of Mazzotta et al. (2004). The

³ <https://github.com/jdonnert/Smac2>

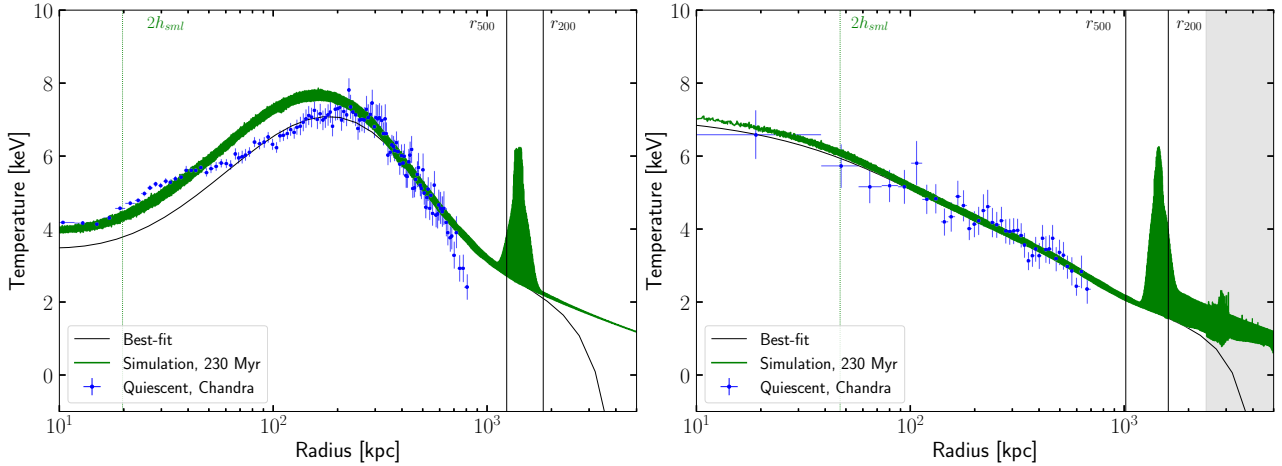


Figure 6. Temperature structure of the $X_E = 0.50$ simulation after 230 Myr. *Left:* fiducial CygA overplotted on the quiescent temperature profile of CygA. For clarity we also show the best-fit model (dotted line). *Right:* fiducial and observed CygNW.

X-ray surface brightness can then be compared to the left panel of Figure 1, and the temperature to the right panel. Based on comparison by eye we can already exclude inclination angles smaller than 30° and larger than 45° because the resulting merger-induced heating is higher, respectively, lower than observed. We further investigate which simulation snapshot could best-represent the Cygnus cluster by generating residual maps for every combination of the zero-energy orbit fraction X_E and the inclination i . These two-dimensional residuals are then folded into a one-dimensional residual histogram to quantitatively identify the ‘best fit’ snapshot. The combination of $X_E = 0.25$ and $i = 30 - 45$ seems to fits the Cygnus cluster best as their histograms are centered closest to zero and have the smallest width. However, we are unable to accurately distinguish between the three different initial velocities.

5.2 Best fit simulation snapshot

We show a map of residuals for $X_E = 0.25$ and $i = 30$ in Figure 8 (left). This particular snapshot has a projected core separation of 765.22 kpc at $T = 1.59$ Gyr after starting the simulation, and is ~ 270 Myr prior to core passage. We zoom into the simulation box to ensure the physical dimensions are equal to the box size of Figure 1, and ensure that the centroids of CygA and fiducial CygA are located at the same point in the image. We then subtract the simulated temperature from the observation, divide by the simulation and multiply by one hundred.

Blue colors denote locations of lower simulated temperature, while red indicates a higher observed temperature. The red dot indicates the location of CygA, and the red blob in the upper right (north west) shows that CygNW is hotter in the observations than in the simulations. We find excess temperature structure in the observations that is not due to the hydrostatic temperature structure of the ICM. For example, we see an arc-like structure (the dark red bin in the bottom left corner). Note, however, that this region is underexposed as most of the *Chandra* pointings are on the region directly surrounding CygA. Furthermore, we find excess temperature towards the left of CygA, as well

as along the presumed merger axis. We further investigate the interstitial region between CygA and CygNW to look for indications of a merger shock at the interface between both clusters in Section 5.4.

Furthermore, we extract radial profiles for the haloes that represent CygA and CygNW in the best fit simulation snapshot. We use wedges of equal boundary angles as used for the observation. This provides us with the quiescent and merger radial profiles (the latter for CygA only) as shown in Figure 9.

5.3 SZ Compton-y Map

We compute the expected [Sunyaev & Zeldovich \(1972, 1980\)](#) Compton-y parameter, shown in Figure 8 (right). Here we overplot the logarithm of the observed *Chandra* X-ray contours. Cygnus A is the brightest extragalactic radio source in the local Universe so a rather high dynamic range will be needed to observe any other radio emission in the vicinity of Cygnus A that is not related to the FR-II source. At present no independent Compton-y measurement of the Cygnus cluster is available in the literature, to our knowledge.

5.4 Shock & compression

We investigate the interface region between both merging cluster haloes to look for signs of merger shocks and associated merger-induced shock heating during the approach prior to core passage. We use the built-in shock finder ([Beck et al. 2016b](#)) to obtain Mach numbers and shock speeds for the SPH particles. The shock finder picks up less than several hundred shocked particles after numerical artefacts from the initial conditions have settled (at $T \gtrsim 1$ Gyr) but prior to core passage ($T < 1.88$ Gyr). We find significant numbers of shocked SPH particles (10^{4-5}) after core passage.

Furthermore, we check whether the Rankine-Hugoniot jump conditions are fulfilled for fluid elements located within a cylinder of radius 150 kpc placed along the merger axis (centered on the interface between both merging haloes). In Fig. 10 we show the mean temperature, density and velocity

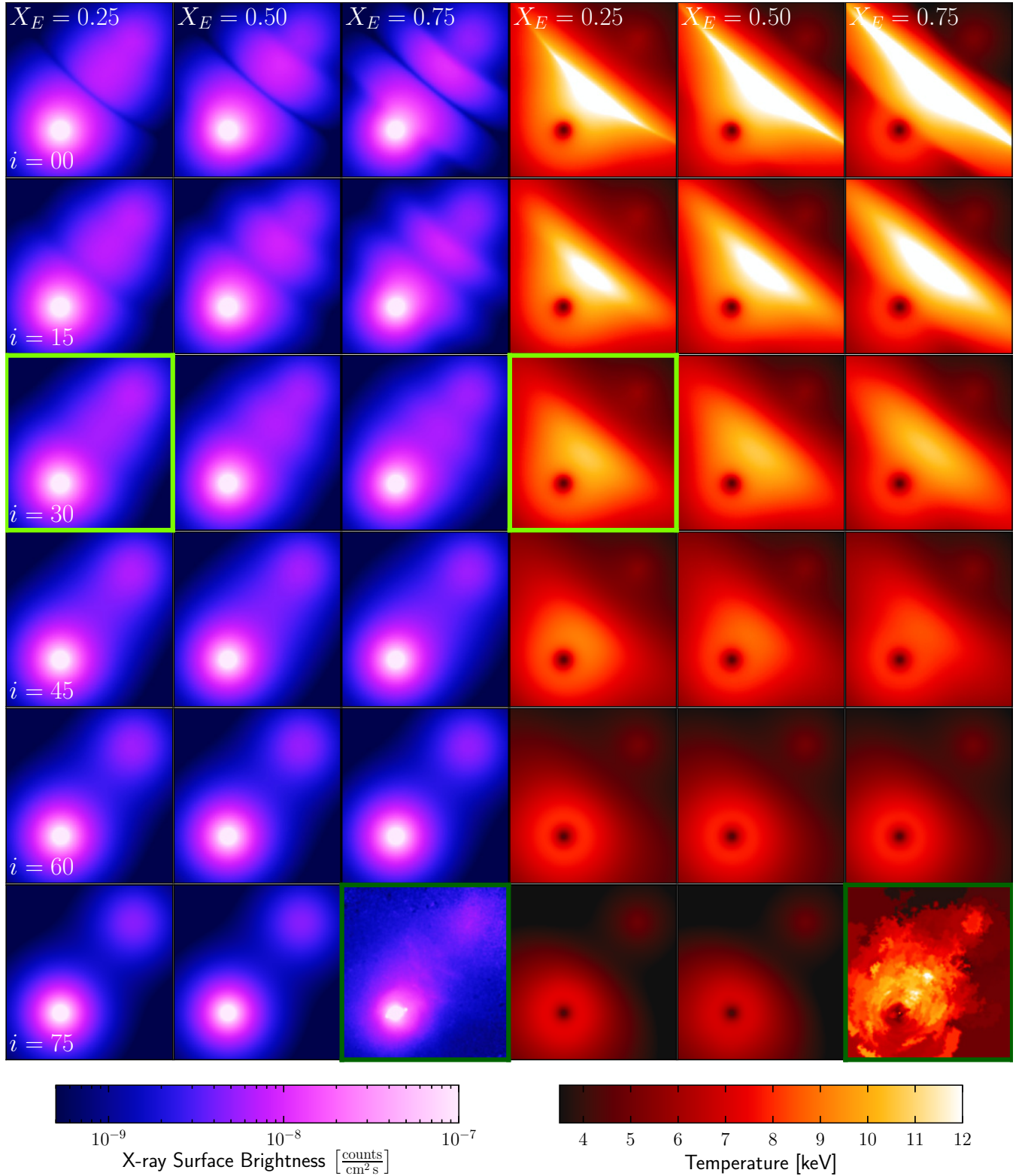


Figure 7. Initial velocity (parametrized by X_E) versus inclination angle i in degrees. *Left:* X-ray Surface Brightness, *Right:* Spectroscopic Temperature. The projected core separation in all panels is 765 ± 15 kpc. The light green panels show our best fit model, and the observation is framed in dark green at the lower right for comparison.

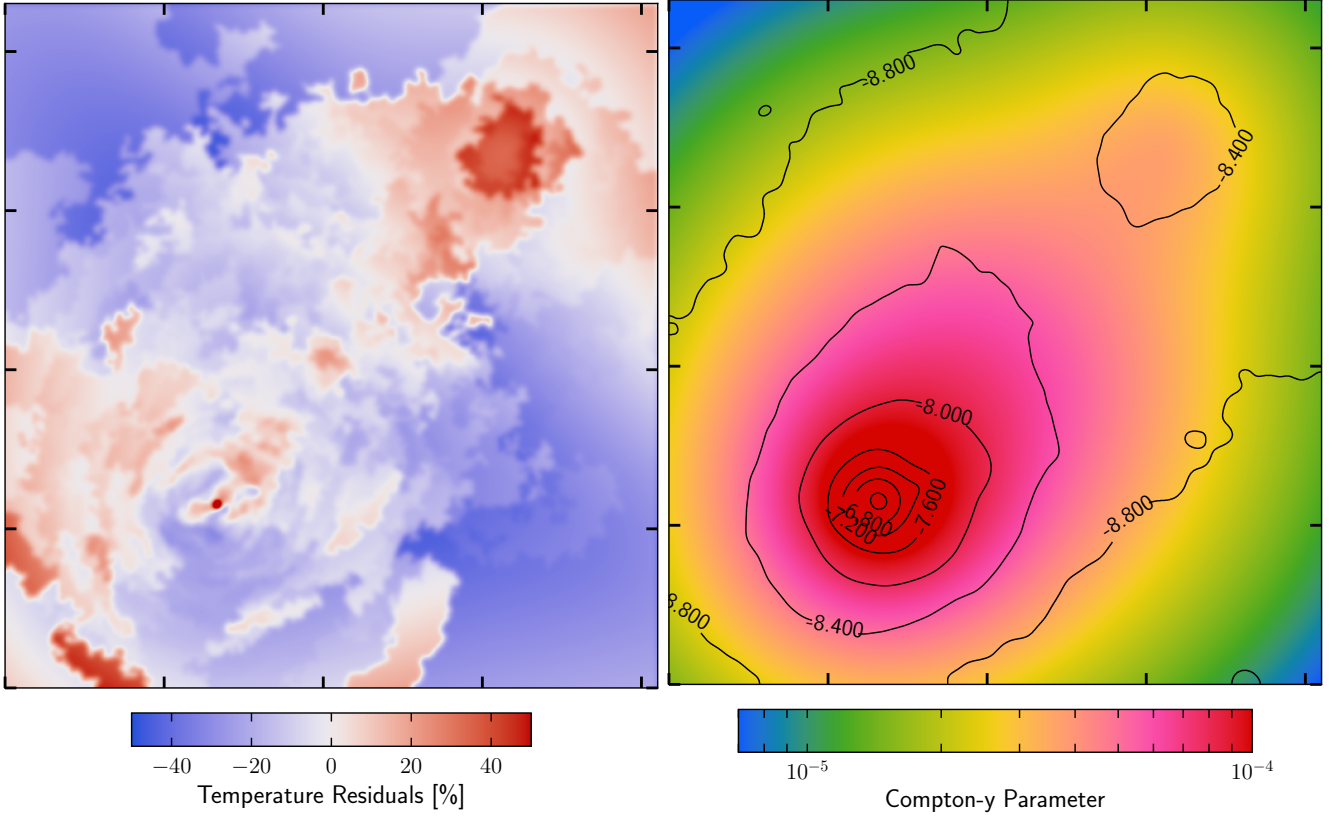


Figure 8. Our best fit $X_E = 0.25$ and $i = 30^\circ$ simulation. *Left:* Temperature residuals. Red indicates the observed temperature is higher than the simulation, conversely, blue indicates a lower observed temperature. *Right:* Compton-y parameter. In contours the X-ray surface brightness in log (counts/cm²/s) as observed by *Chandra*.

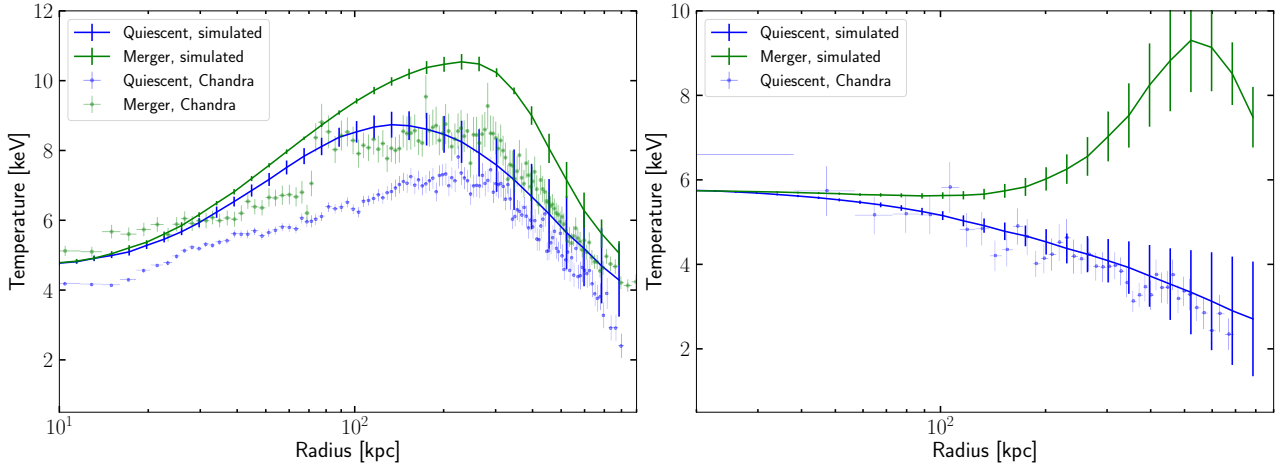


Figure 9. Temperature profiles of the $X_E = 0.25$, $i = 30^\circ$ simulation after 1.59 Myr with a core separation of 765.22 kpc. The ‘quiescent’ wedge is shown in blue while the ‘merger’ wedge is depicted in green. *Left:* fiducial CygA overlotted on the quiescent temperature profile of CygA. *Right:* fiducial and observed CygNW.

within this cylinder at four different time steps. We observe no discontinuity in density, temperature or velocity in the boundary region between the two clusters.

Finally, we show the SPH velocity divergence (in arbitrary units) of the bestfit simulation snapshot ($X_E = 0.25$ at $T=1.59$ Gyr) in Fig. 11. The sign is negative everywhere within this image and white [blue] indicates where compression is strongest [weakest]. The panel on the left shows a

projected picture for the bestfit $i = 30^\circ$ inclination angle. The panel on the right shows the same simulation snapshot, but de-projected ($i = 0^\circ$), and de-rotated within the xy -plane (with angle 51° measured from west to the north).

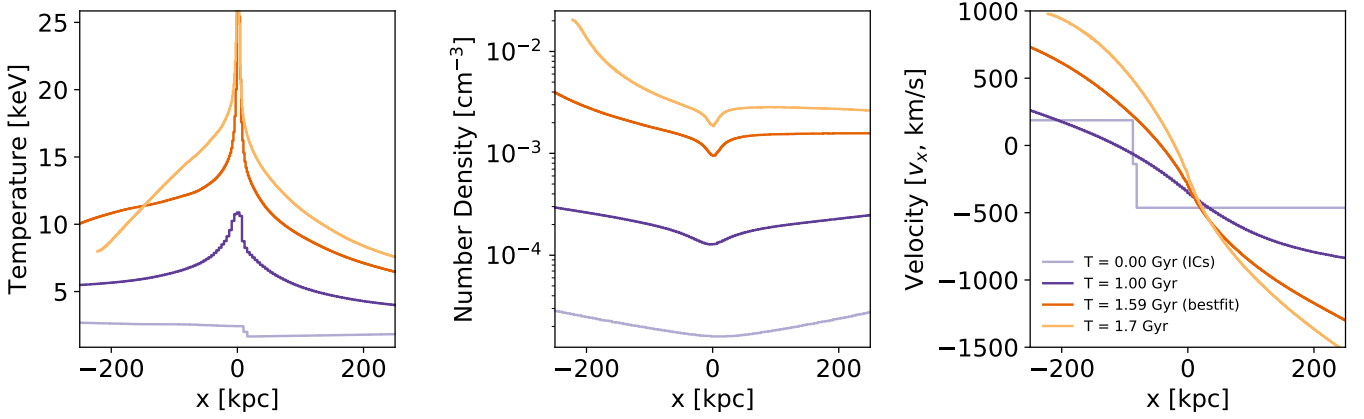


Figure 10. Temperature, density and velocity of SPH particles inside a cylinder of radius 150 kpc located along the merger axis and centered at the interface between both haloes.

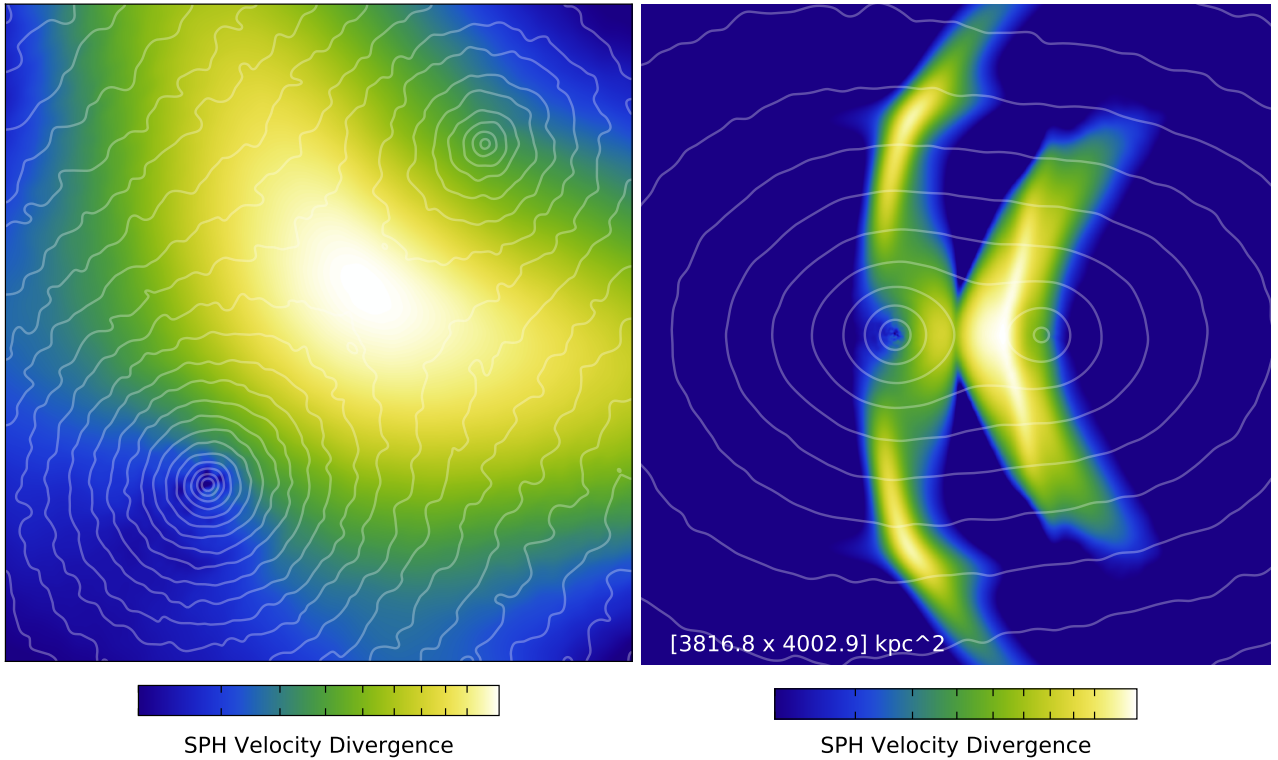


Figure 11. SPH velocity divergence (arbitrary units) for the bestfit snapshot of the $X_E = 0.25$ and $i = 30^\circ$ simulation. The sign of the velocity divergence is negative, indicating where compression in the interstitial region occurs and is strongest (white). Contour lines show the dark matter density and are included to indicate where both haloes can be found (levels differ between both panels). To emphasize, both panels are generated using the same simulation snapshot, but viewed from different angles. *Left:* Projected ($i = 30^\circ$), and rotated (51°) map. *Right:* De-projected ($i = 0^\circ$) picture where the merger-axis is horizontal (i.e. the simulation box is rotated in the xy -plane with respect to the left panel with angle -51° measured from west to the north).

6 DISCUSSION

The baryonic profiles of CygA and CygNW are constrained by two megaseconds of *Chandra* observations of the ICM, and we derive the dark matter profile under the assumption of hydrostatic equilibrium and spherical symmetry.

6.1 Concentration parameter

The *Chandra* observation span a radius range of 50-100 kpc for the cluster haloes of both CygA and CygNW. Modelling the cluster environment gives virial radii of >1500 kpc. This is well outside of the observed data range and indicates that the virial radii of CygA and CygNW overlap significantly as the observed core separation is $701.3'' \sim (765 h_{70}^{-1} \text{ kpc})$. This makes it difficult to infer the scaling radius r_s (the

turnover point in the NFW slope from -1 to -3), and influences the inferred concentration parameter. Moreover, this implies that the progenitor clusters have a total gravitating mass M_{200} at the virial radius such that the mass-ratio is of order $1.5 : 1$. Note, however, that we assume spherical symmetry for both cluster haloes. A more realistic scenario is that the cluster haloes are triaxial and elongated along the cosmic filament, particularly in the scenario of a major merger. The spatial baryon distribution in CygNW might hint to elongation towards CygA. Assuming spherical symmetry could result in an uncertainty of the mass-estimate by up to a factor two (e.g. Corless & King 2007) and could change the true mass ratio significantly.

6.2 Cut-off radii

The inferred cluster parameters are furthermore influenced by the cut-off in the density profiles. It is particularly difficult to constrain the cut-off radius. We find values that lie well outside the domain of our observations. Even if the cut-off radius would lie within 1 Mpc, low-photon counts and a large surface area in the outskirts of the cluster make for low-number statistics or an infeasibly large observation time. In addition, this would require correcting for non-trivial systematic background errors. D17 reports a cut-off radius of 1.7 times the virial radius R_{200} for the Perseus cluster, while our best fit for the Cygnus cluster shows a cut-off smaller than the virial radius. Cutting the density results in a slightly lower baryon fraction and concentration parameter and a higher total mass than a model without an additional cut-off in the density profiles.

6.3 Increasing central temperature

Given our best fit cluster parameters we set up initial conditions that faithfully represent the observed cluster state in the beginning of the simulation. When the haloes are simulated separately in a box with periodic boundaries, we find that the profiles remain very stable for over 5 Gyr. When both clusters are placed on a merger trajectory in the same box, however, a rapid increase in the central temperature is noticed during the first ~ 200 Myr. We interpret this as the result of tidal interaction between both halos. We note that an equilibrium with a slightly higher central temperature is reached that remains close to the observed *Chandra* profiles. In addition, we notice that the scatter of the simulated temperature around the analytical profile increases over the course of the simulation run. We interpret this behaviour as an artefact of the particular SPH formulation used: numerical imprecision mostly affects the internal energy (from which the temperature is computed) and accumulates over the course of the GADGET3 run.

6.4 Best fit simulation snapshot

We investigate the effect of increasing the initial velocity, parametrized by the zero-energy orbit fraction X_E , as well as changing the orientation of the system on the sky by varying the inclination i , shown in Figure 7. The inclination is defined as zero when the merger occurs in the plane of the sky while a value of 90° corresponds to a merger along the

line of sight. As two distinct cluster haloes are visible the latter is ruled out. Prior literature values are 54° (Sarazin et al. 2013) or $30 - 45^\circ$ (Ledlow et al. 2005) from dynamical modeling. The true physical distance increases with inclination, thus simulated time decreases. Therefore the amount of merger heating will be lower with increasing inclination. We use this to resolve the time-angle degeneracy. Inclination angles outside the range $30 - 45^\circ$ can certainly be ruled out because the amount of merger-induced heating is either much larger, or non-existent for smaller or larger inclination angles, respectively.

It is, however, very difficult to obtain a more precise value for the inclination angle or to differentiate between different merger velocities. We show radial temperature profiles in Fig. 9, and two-dimensional residuals map as well as the expected SZ signal for the $X_E = 0.25$ and $i = 30^\circ$ simulation in Fig. 8. Observing a distinct merger shock and quantifying it with an estimate of the Mach number would allow further constraints on the merger velocity and inclination angle. Furthermore, radially averaging the observed temperature profile could wash out the temperature structure at larger radii because the bins span a larger area where part of the merger-enhanced temperature structure is averaged with lower-temperature gas that has not been affected as much by the ongoing merger.

We now turn to the residuals map of the temperature structure in Figure 8 (left). The remaining temperature structure is neither the hydrostatic temperature of the intracluster medium, nor merger-heated gas. CygNW appears hotter in the observations, but the innermost data point falls below the resolution limit of our simulations. Therefore the temperature in the innermost region of CygNW is not well represented in our simulations. The residuals surrounding CygA, on the other hand, are certainly resolved numerically and show residual temperature structure. These radii correspond to the temperature jumps in the radial temperature profile of Figure 9 (left). Although the temperature profile in the inner region ‘creeps up’, the overall radial temperature profile of the ‘quiescent’ and ‘merger-enhanced’ region are much smoother in the simulation than in the observation. We suggest that the excess heating could be due to AGN activity over the past hundreds of mega years, and could be turned quantitatively to an estimate of the energy output of Cygnus A. Assuming that the AGN outflow travels outward with the local speed of sound, the distance can be used as a proxy for time of the outburst. See Wise et al. (in prep).

6.5 Shocks & compression

We see no indications for a merger shock in the Cygnus cluster in Fig. 10. The density, temperature, and velocity increase smoothly over time, except for artificial discontinuities in the initial conditions that settle within the first Gyr. The presence of a shock would require that the fluid satisfies the Rankine-Hugoniot jump conditions. However, we observe no such discontinuities. Furthermore, we notice that the velocity changes sign at the interface region $x = 0$. This suggests that the merger is not yet driving shocks into the ICM, and that the merger-induced heating of the ICM as seen in Fig. 7 (three columns on the right) is the result of compression. Therefore we show the SPH velocity divergence in Fig. 11 to further illustrate where compression occurs and

is strongest. The location of the largest magnitude of the velocity field (white colours) correlates exactly with the region of highest merger-enhanced temperature in the ICM.

In addition, the non-detection of shocked SPH particles in the interface region between $1 \lesssim T < 1.88$ Gyr further strengthens the view that we do not see a merger shock in-between CygA and CygNW. Within this time frame only several hundred SPH-particles are picked up by the shock finder, which is significantly less than the number of neighbours required to sample the SPH kernel properly. We do not find a merger shock in-between both cluster centroids regardless of the exact inclination angle of the merger. The observed (projected) core separation of $765 h_{70}^{-1}$ kpc in the $X_E = 0.25$ simulation is reached at times between $T = 1.31 - 1.63$ Gyr for inclination angles $60 - 0$ degrees, which falls within the time range where we find only several hundred shocked particles.

A strong axial shock does develop ahead of the dark matter core of the halo that represents CygA immediately after core passage, which occurs at $T = 1.88$ Gyr for the $X_E = 0.25$ simulation. This shock is numerically very well resolved by at least 12.000 SPH particles (when the shock first forms), up to well over 100.000 particles at later times. However, the post core-passage scenario is of no physical interest to the pre-merger Cygnus cluster.

The development of merger shocks in our simulations is consistent with the recent study involving cosmological simulations of [Ha et al. \(2018\)](#), where the authors studied the development of merger shocks in (near) head-on merger simulations of mass ratio $2 : 1$. However, we find no equatorial shocks as a result of our initial conditions setup: we do not correctly sample the background density of the cosmic filament in the simulation box, and our simulations start after or at the time these shocks would (start to) form.

7 CONCLUSIONS

We ran state of the art (idealised) binary merger simulations of the ongoing merger and draw the following conclusions.

- CygA is surrounded by a dark matter halo that is more massive and more concentrated than expected for a typical cluster of galaxies. The inferred concentration parameter is a significant outlier in the [Duffy et al. \(2008\)](#) scatter relation of c_{NFW} versus M_{200} . The estimated baryon fraction is well below ten per cent (where we expect a total baryon fraction of seventeen per cent for a typical cluster). The exact value, however, strongly depends on the particular value inferred for the cut-off radius.

- We interpret the low fraction of baryons in the intracluster medium as an indication that a higher fraction of baryons has cooled sufficiently to settle into the cluster galaxies, particularly the brightest cluster galaxy. This may have resulted in a higher star formation rate and/or more baryons present in the interstellar medium of the Cygnus A galaxy and could explain the persistent high output power of the active galactic nucleus as more fuel is available in the Cygnus A galaxy than in typical brightest cluster galaxies.

- Modeling the data suggests that the CygNW subcluster has a total gravitating mass at the virial radius that is roughly equal to the total mass in CygA. CygNW appears much fainter in the X-ray surface brightness than

CygA, so we would intuitively expect CygA to be much more massive. The X-ray surface brightness, however, scales with $\sqrt{T} \cdot \rho_0^2$, where the central density ρ_0 is an order of magnitude lower for CygNW than for CygA. The high temperature of CygNW, on the other hand, could be indicative of the high mass as the initial conversion from potential to thermal energy depends on the mass.

- Our simulations show a best fit snapshot with an inclination of $30 - 45^\circ$, consistent with the dynamical model of [Ledlow et al. \(2005\)](#). However, the X-ray observations show a core separation of $765 h_{70}^{-1}$ kpc rather than the value of $400 h_{75}^{-1}$ kpc found there.

- We find a total gravitating mass of $7.36 \cdot 10^{14} M_\odot$ for CygA and $4.99 \cdot 10^{14} M_\odot$ for CygNW. The mass of both subclusters found by dynamical modeling of $2 \cdot 10^{15} M_\odot$ is an order of magnitude higher than found using the X-ray observations. Numerical simulations with such a high cluster mass would be inconsistent with the *Chandra* observations.

- We find no signs of a merger shock in-between CygA and CygNW and suggest that the merger heats the ICM due to compression. We subtract the simulated temperature structure of the Cygnus cluster from the observations to generate a two-dimensional map of residual temperature structure that is neither due to the hydrostatic temperature structure nor due to merger-induced heating of the gas.

ACKNOWLEDGEMENTS

We would like to thank the anonymous referee for their useful comments on the draft version of this paper. The scientific results reported in this article are based on observations made by the Chandra X-ray Observatory. We thank Klaus Dolag and Volker Springel for access to the proprietary version of the code GADGET3. We thank SURFsara (www.surfsara.nl) for the support in using the Lisa Compute Cluster, and the Max Planck Computing and Data Facility for maintaining the Freya compute cluster. JD was supported by the People Programme (Marie Skłodowska Curie Actions) of the European Union Eighth Framework Programme H2020 under REA grant agreement no 658912, “Cosmo Plasmas”. TLRH acknowledges support from the International Max-Planck Research School (IMPRS) on Astrophysics. TLRH thanks Alex Arth and Ulrich Steinwandel for useful discussions and help with resimulating P-GADGET3 snapshots for finer interpolation. Plots were generated using MATPLOTLIB ([Hunter 2007](#)), and the two-dimensional figures in this paper use the perceptually uniform colour maps of [Kovesi \(2015\)](#). This research made use of NUMPY ([Van Der Walt et al. 2011](#)), SCIPY ([Jones et al. 2001](#)), ASTROPY ([Astropy Collaboration et al. 2013](#)), and APLPY, an open-source plotting package for PYTHON hosted at <http://aplp.py.github.com>.

REFERENCES

- Arnaud K. A., Fabian A. C., Eales S. A., Jones C., Forman W., 1984, *MNRAS*, **211**, 981
- Arnaud K. A., Johnstone R. M., Fabian A. C., Crawford C. S., Nulsen P. E. J., Shafer R. A., Mushotzky R. F., 1987, *MNRAS*, **227**, 241

- Astropy Collaboration et al., 2013, *A&A*, **558**, A33
- Bartelmann M., Steinmetz M., 1996, *MNRAS*, **283**, 431
- Beck A. M., et al., 2016a, *MNRAS*, **455**, 2110
- Beck A. M., Dolag K., Donnert J. M. F., 2016b, *MNRAS*, **458**, 2080
- Carilli C. L., Barthel P. D., 1996, *A&ARv*, **7**, 1
- Carilli C. L., Harris D. E., 1996, Cygnus A – Study of a Radio Galaxy
- Carilli C. L., Perley R. A., Harris D. E., 1994, *MNRAS*, **270**, 173
- Cavaliere A., Fusco-Femiano R., 1978, *A&A*, **70**, 677
- Chon G., Böhringer H., Krause M., Trümper J., 2012, *A&A*, **545**, L3
- Corless V. L., King L. J., 2007, *MNRAS*, **380**, 149
- Dehnen W., Aly H., 2012, *MNRAS*, **425**, 1068
- Dickey J. M., Lockman F. J., 1990, *ARA&A*, **28**, 215
- Diehl S., Rockefeller G., Fryer C. L., Riethmiller D., Statler T. S., 2012, preprint, ([arXiv:1211.0525](https://arxiv.org/abs/1211.0525))
- Dolag K., Staszczyn F., 2009, *MNRAS*, **398**, 1678
- Donnert J. M. F., 2014, *MNRAS*, **438**, 1971
- Donnert J., Brunetti G., 2014, *MNRAS*, **443**, 3564
- Donnert J. M. F., Beck A. M., Dolag K., Röttgering H. J. A., 2017, *MNRAS*, **471**, 4587
- Duffy A. R., Schaye J., Kay S. T., Dalla Vecchia C., 2008, *MNRAS*, **390**, L64
- Fabbiano G., Schwartz D. A., Schwarz J., Doxsey R. E., Johnston M., 1979, *ApJ*, **230**, L67
- Fabricant D., Lecar M., Gorenstein P., 1980, *ApJ*, **241**, 552
- Freeman P., Doe S., Siemiginowska A., 2001, in Starck J.-L., Murtagh F. D., eds, Proc. SPIE Vol. 4477, Astronomical Data Analysis. pp 76–87 ([arXiv:astro-ph/0108426](https://arxiv.org/abs/astro-ph/0108426)), [doi:10.1117/12.447161](https://doi.org/10.1117/12.447161)
- Fruscione A., et al., 2006, in Society of Photo-Optical Instrumentation Engineers (SPIE) Conference Series. p. 62701V, [doi:10.1117/12.671760](https://doi.org/10.1117/12.671760)
- Giacconi R., Murray S., Gursky H., Kellogg E., Schreier E., Tananbaum H., 1972, *ApJ*, **178**, 281
- Ha J.-H., Ryu D., Kang H., 2018, *ApJ*, **857**, 26
- Hunter J. D., 2007, Computing In Science & Engineering, **9**, 90
- Jones E., Oliphant T., Peterson P., Others 2001, SciPy: Open source scientific tools for Python, <http://www.scipy.org/>
- Kalberla P. M. W., Burton W. B., Hartmann D., Arnal E. M., Bajaja E., Morras R., Pöppel W. G. L., 2005, *A&A*, **440**, 775
- Kovesi P., 2015, preprint, ([arXiv:1509.03700](https://arxiv.org/abs/1509.03700))
- Ledlow M. J., Owen F. N., Miller N. A., 2005, *AJ*, **130**, 47
- Markevitch M., Sarazin C. L., Vikhlinin A., 1999, *ApJ*, **521**, 526
- Mazzotta P., Rasia E., Moscardini L., Tormen G., 2004, *MNRAS*, **354**, 10
- McKean J. P., et al., 2016, *MNRAS*, **463**, 3143
- Navarro J. F., Frenk C. S., White S. D. M., 1995, *MNRAS*, **275**, 720
- Owen F. N., Ledlow M. J., Morrison G. E., Hill J. M., 1997, *ApJ*, **488**, L15
- Perley D. A., Perley R. A., Carilli C. L., 2016, The Astronomer’s Telegram, **9495**
- Sanders J. S., 2006, *MNRAS*, **371**, 829
- Sarazin C. L., Finoguenov A., Wik D. R., 2013, *Astronomische Nachrichten*, **334**, 346
- Smith R. K., Brickhouse N. S., Liedahl D. A., Raymond J. C., 2001, *ApJ*, **556**, L91
- Smith D. A., Wilson A. S., Arnaud K. A., Terashima Y., Young A. J., 2002, *ApJ*, **565**, 195
- Somerville R. S., Davé R., 2015, *ARA&A*, **53**, 51
- Springel V., 2005, *MNRAS*, **364**, 1105
- Steenbrugge K. C., Blundell K. M., Duffy P., 2008, *MNRAS*, **388**, 1465
- Sunyaev R. A., Zeldovich Y. B., 1972, Comments on Astrophysics and Space Physics, **4**, 173
- Sunyaev R. A., Zeldovich I. B., 1980, *ARA&A*, **18**, 537
- Tadhunter C., Marconi A., Axon D., Wills K., Robinson T. G., Jackson N., 2003, *MNRAS*, **342**, 861
- Van Der Walt S., Colbert S. C., Varoquaux G., 2011, Computing in Science & Engineering, **13**, 22
- Wilms J., Allen A., McCray R., 2000, *ApJ*, **542**, 914
- Wise M., 2014, The Rise to Power: Half a Billion Years of Intense AGN Activity in the Merging Cluster Cygnus A, Chandra Proposal
- Yaji Y., Tashiro M. S., Isobe N., Kino M., Asada K., Nagai H., Koyama S., Kusunose M., 2010, *ApJ*, **714**, 37
- de Vries M. N., et al., 2018, *MNRAS*, **478**, 4010

This paper has been typeset from a $\text{\TeX}/\text{\LaTeX}$ file prepared by the author.